

E-LMC: Extended Linear Model of Coregionalization for Predictions of Spatial Fields

Shihong Wang

*School of Integrated Circuit Science and Engineering
Beihang University
Beijing, China
wangshihong@buaa.edu.cn*

Xueying Zhang

*School of Integrated Circuit Science and Engineering
Beihang University
Beijing, China
xueying.zhang@buaa.edu.cn*

Yichen Meng

*School of Integrated Circuit Science and Engineering
Beihang University
Beijing, China
mengyc@buaa.edu.cn*

Wei Xing*

*School of Integrated Circuit Science and Engineering
Beihang University
Beijing, China
wxing@buaa.edu.cn*

Abstract—Physical simulations based on partial differential equations typically generate spatial fields results, which are utilized to calculate specific properties of a system for engineering design and optimization. Due to the intensive computational burden of the simulations, a surrogate model mapping the low-dimensional inputs to the spatial fields are commonly built based on a relatively small dataset. To resolve the challenge of predicting the whole spatial field, the popular linear model of coregionalization (LMC) can disentangle complicated correlations within the high-dimensional spatial field outputs and deliver accurate predictions. However, LMC fails if the spatial field cannot be well approximated by a linear combination of base functions with latent processes. In this paper, we extend LMC by introducing an invertible neural network to linearize the highly complex and nonlinear spatial fields such that the LMC can easily generalize to nonlinear problems while preserving the traceability and scalability. Several real-world applications demonstrate that E-LMC can exploit spatial correlations effectively, showing a maximum improvement of about 40% over the original LMC and outperforming the other state-of-the-art spatial field models.

Index Terms—spatial field, high-dimensional output, neural network, Gaussian process, principal component analysis

I. INTRODUCTION

Applications such as design optimization and inverse parameter estimation require repeated solutions to sophisticated partial differential equations (PDEs) [1], [2]. Due to the expensive computation of experiments or simulations, a data-driven surrogate model is frequently built [3]. The surrogate model can be queried cheaply, so it is utilized to replace the original simulator. Popular specific implementations for surrogate models are Gaussian processes, radial basis function, support vector machines, neural networks, and Bayesian networks.

However, simulations of PDEs generally produce high-dimensional spatial or spatial-temporal field results (e.g., velocity, temperature, pressure, or magnetic fields). Thus, such situations demand us to build a surrogate model between

high-dimensional outputs and low-dimensional inputs, from a relatively small number of training samples. Traditional statistical methods become inefficient for problems with high-dimensional outputs, while learning an end-to-end deep learning model directly poses a huge challenge in model complexity and computation cost [4]–[6]. Therefore, it is of great significance to build a proxy of low-to-high mapping, based on a limited number of simulation samples.

In this paper, we develop E-LMC, a novel framework by combining the neural network and the linear model of coregionalization (LMC) to act as a hybrid model for computationally expensive spatial fields defined in high-dimensional output spaces. Neural network helps to disentangle the nonlinear features, whereas LMC linearly integrates base functions with latent processes to model the high-dimensional outputs. Our method can effectively capture the complicated correlations within spatial fields and provide accurate predictions. In theory, our method is a generalization of LMC for highly complex and nonlinear spatial-fields.

Our work makes three main contributions to the high-dimensional spatial field prediction:

- We extend LMC by introducing a general framework to linearize the highly complex and nonlinear outputs such that the LMC can easily generalize to nonlinear problems while preserving the traceability and scalability.
- To introduce a powerful model capacity for the linearization process, we introduce a neural network; for model training, we propose an efficient training algorithm such that E-LMC is always no worse than LMC due to overfitting issues.
- We evaluate the proposed method on two canonical physics-based simulations (cantilever beam topology optimization and metal melting condition prediction). The results demonstrate a significant superiority over the original LMC with a maximum of 40% accuracy improvement and outperform the other state-of-the-art spatial field

models.

The remainder of this paper is structured as follows: Section II reviews the related work of the surrogate model in high-dimensional spatial field prediction; Section III presents the construction of the proposed E-LMC model; Section IV describes the implementation details and illustrates our results; finally, conclusions for the whole paper and future work are drawn in Section V.

II. RELATED WORK

A. Learning the Spatial Field

For physical simulations based on PDEs, the output is a spatial field, normally represented using its values on a regular grid. In this situation, the dimensionality of the output space is equal to the number of points in the spatial grid. Calculations of high-dimensional spatial fields are usually performed through the finite element/difference methods, and both of them are computationally intensive. To conduct efficient analysis for engineering and scientific purposes, an efficient way to reduce the high demand is to incorporate surrogate models, which are essentially regression models, such as conservation kernels [7] and hybrid physics-based data-driven surrogates [8].

From the data-driven surrogate perspective, deep neural network (DNN) can be used to construct supervised models for numerical simulators. Multilayer perceptron (MLP), a typical example of DNN, is capable of effectively recovering a low-dimensional nonlinear manifold in high-dimensional data [9]–[11]. However, these end-to-end neural network methods or deep learning hybrid methods require massive tuning and are prone to overfitting [12], [13]. Thus, single neural network modeling is not suitable for modeling of the spatial fields.

B. Gaussian Process for Spatial Field Prediction

As a nonparametric method that can adopt prior knowledge and provide uncertainty quantification, Gaussian process (GP) is frequently used as the data-driven surrogate model [14]–[16]. GP can alleviate overfitting and automatically capture the complexity of the functions underlying the data, from a limited number of training sets. In recent decades, GP has been used for various kinds of tasks, including face detection [17], collaborative filtering [18], and optimization [19].

Unfortunately, GP cannot be naturally extended to learn a function with multiple outputs, especially in the high-dimensional spatial fields. It is hard to apply GP to computational physics directly. Additionally, there are strong and complex correlations among the spatial outputs. If we ignore output correlations and simply treat each output independently (given inputs), it is likely to result in severe overfitting, particularly for small datasets. Therefore, multi-output GP models have been proposed to capture the output correlations. For example, the convolved GP models the covariance among the outputs through convolution operations [20], [21]. PCA-GP [4], Isomap-GP [5], and kPCA-GP [6] assume a low-rank structure within the outputs and then model the mapping of this low-rank structure to the inputs, through a linear combination

of a group of fixed bases. Regardless of their effectiveness, for a general GP, the computational complexity is $\mathcal{O}(N^3 d^3)$, where N is the number of training samples and d is the output dimensionality [22]. As the number of required training samples grows drastically for a highly nonlinear response surface, the idea of single surrogate modeling becomes less practical.

In summary, the aforementioned surrogate models are either impractical for large spatial fields or inadequate to capture complicated correlations among very high-dimensional spatial outputs.

C. Dimensionality Reduction in Spatial Field Prediction

As large datasets are becoming more widely used in various fields, the necessity for dimensionality reduction of complex data, especially high-dimensional datasets, is growing exponentially [23]. Typically, dimensionality reduction is defined as the mapping of high-dimensional data into a low-dimensional representation [24]. Lower dimensions mean less computation, less memory, and faster learning. Dimensionality reduction can extract the hidden information and analyze the underlying structure. As a common way of preprocessing, it reduces the computation cost of machine learning algorithms by decreasing the complexity of training [25]. It is also expected to improve the model accuracy by relieving overfitting.

Implementations of dimensionality reduction can be classified into linear and nonlinear methods [26]. Principal component analysis (PCA) is one of the most widely used and scalable linear dimensionality reduction techniques. The purpose of PCA is to decompose the original data with a few linearly uncorrelated variables based on an affine transformation. By projecting each data point onto the first few principal components, lower-dimensional data are obtained while preserving as much of the data's variation as possible. The principal components are often computed using eigendecomposition of the data covariance matrix or singular value decomposition (SVD) of the data matrix. Due to the unsupervised nature of PCA, the underlying structure of high-dimensional data can be elucidated without prior information. This property facilitates data analysis or other applications. For example, machine learning algorithms with PCA produce better results when dimensionality of the datasets is high [27], [28]. In cases of low data volume, PCA offers better stability and generalization compared with neural networks such as autoencoder, which is first initialized randomly and then optimized iteratively.

However, the capability of PCA to handle data with nonlinear relationships is limited. Most physical or chemical processes in the real world generate nonlinear data. To deal with such a circumstance, neural networks are frequently utilized.

The potential of a neural network resides in nonlinearity, allowing the model to learn more powerful generalizations compared to PCA [29]. It is known that a neural network with a linear activation function can learn the principal component representation of the input data [30]. There are also approaches to turn a PCA into an autoencoder, by generating an encoder

layer using the PCA parameters and adding a decoding layer. This can be implemented by a fully-connected neural network [31] or a convolutional neural network [32]. But the weights of the autoencoder are not equal to principal components, and are generally not orthogonal. Using PCA to initialize MLP allows for less training data while achieving decent performance [31]. Furthermore, unlike ordinary datasets, data from PDEs are often high-dimensional spatial fields which have limited amount. So the direct use of MLP cannot reconstruct or extract efficiently, leading to overfitting. Therefore, combining PCA with MLP may be beneficial to such an issue. PCA can increase the stability of the features learned by MLP because PCA requires few samples.

III. METHOD

A. Statement of the Problem

The predictions of the spatial field (usually produced from the simulation) can be considered as approximating an injective mapping $\mathbf{f} : \mathcal{X} \rightarrow \mathcal{M}$, where $\mathcal{M} \subset \mathbb{R}^d$ is the permissible output space (response surface) and $\mathcal{X} \subset \mathbb{R}^l$ is the permissible input space. That is, $\mathbf{f}(\mathbf{x}) = \mathbf{y} = (u(\mathbf{x}^{(1)}; \mathbf{x}), \dots, u(\mathbf{x}^{(d)}; \mathbf{x}))^T$ for an arbitrary input \mathbf{x} . The objective of statistical emulation is to approximate the mapping \mathbf{f} for a given set of *training points* $\mathbf{y}^{(j)} = \mathbf{f}(\mathbf{x}^{(j)}) \in \mathcal{M}$, $j = 1, \dots, m$. The corresponding inputs $\mathbf{x}^{(j)} \in \mathcal{X}$ are referred to as *design inputs*.

B. Overview

As shown in Fig. 1, E-LMC consists of the MLP module and the LMC module. The first step of the MLP module disentangles the nonlinearity of the high-dimensional spatial outputs. Thus, we capture the relationship among outputs and find a subspace of spatial output space leading to an optimal representation of the LMC model response surface. Following that, we employ PCA and GP to implement the LMC module, which maps the inputs and the low-dimensional representations. Finally, with inverse PCA and the second step of the MLP module, we can reconstruct the linear and nonlinear characteristics to obtain the prediction.

We begin by introducing the basic GP model for scalar-valued high-dimensional spatial outputs. We then present the LMC module and an efficient implementation of it. Finally, we provide the MLP modules and propose the workflow algorithm of the E-LMC.

C. Gaussian Process Regression

Traditional surrogate models address this problem by utilizing data generated from a few accurate simulations. For simplicity, consider the number of variables to be univariate. The *prior distribution* over the function $\mathbf{f}(\mathbf{x})$ in a GP model:

$$\mathbf{f}(\mathbf{x})|\boldsymbol{\theta} \sim \mathcal{GP}(m(\mathbf{x}), c(\mathbf{x}, \mathbf{x}'|\boldsymbol{\theta})) \quad (1)$$

where the notation denotes that $\mathbf{f}(\mathbf{x})$ is distributed according to a GP, with mean and covariance functions $m_0(\mathbf{x})$ and $c(\mathbf{x}, \mathbf{x}'|\boldsymbol{\theta})$, in which $\boldsymbol{\theta}$ is a vector of (usually unknown) hyperparameters associated with the covariance function of a

given functional form. The prior (1) is updated using available data to obtain a posterior predictive GP distribution, with revised mean and covariance functions conditioned on $\boldsymbol{\theta}$ [33]:

$$\begin{aligned} \mathbf{f}(\mathbf{x})|\mathbf{t}, \boldsymbol{\theta} &\sim \mathcal{GP}(m'(\mathbf{x}|\boldsymbol{\theta}), c'(\mathbf{x}, \mathbf{x}'|\boldsymbol{\theta})) \\ m'(\mathbf{x}|\boldsymbol{\theta}) &= \mathbf{c}(\mathbf{x})^T \mathbf{C}(\boldsymbol{\theta})^{-1} \mathbf{t} \\ c'(\mathbf{x}, \mathbf{x}'|\boldsymbol{\theta}) &= c(\mathbf{x}, \mathbf{x}'|\boldsymbol{\theta}) - \mathbf{c}(\mathbf{x})^T \mathbf{C}(\boldsymbol{\theta})^{-1} \mathbf{c}(\mathbf{x}') \end{aligned} \quad (2)$$

where $\mathbf{t} = (y_1, \dots, y_M)^T$, $\mathbf{C}(\boldsymbol{\theta}) = [C_{ij}]$, in which $C_{ij} = c(\mathbf{x}_i, \mathbf{x}_j|\boldsymbol{\theta})$, $i, j = 1, \dots, M$, is the covariance matrix and $\mathbf{c}(\mathbf{x}) = (c(\mathbf{x}_1, \mathbf{x}|\boldsymbol{\theta}), \dots, c(\mathbf{x}_M, \mathbf{x}|\boldsymbol{\theta}))^T$. The expected value $\mathbb{E}[\mathbf{f}(\mathbf{x})]$ is given by $m'(\mathbf{x}|\boldsymbol{\theta})$ and $c'(\mathbf{x}, \mathbf{x}'|\boldsymbol{\theta})$ is the predictive variance. The hyperparameters $\boldsymbol{\theta}$ can be obtained from the maximum log-likelihood estimate [34].

D. Linear Model of Coregionalization (LMC)

The basic GP does not naturally extend to spatial output problems. There are several ways to extend this approach to multivariate cases, which fall into the general framework of the linear model of coregionalization.

Consider one of the outputs $\mathbf{f}(\mathbf{x}) \in \mathbb{R}^D$, LMC assumes that the coordinates $f_d(\mathbf{x})$, $d = 1, \dots, D$, of $\mathbf{f}(\mathbf{x})$ are linear combinations of Q GPs (or, more generally, random functions):

$$f_d(\mathbf{x}) = \sum_{q=1}^Q \sum_{i=1}^{R_q} a_{d,q}^i u_q^i(\mathbf{x}) \quad (3)$$

where $a_{d,q}^i$ are scalar coefficients and $u_q^i(\mathbf{x})$ are zero mean, unit-variance GPs that are related by $\text{cov}(u_q^i(\mathbf{x}), u_{q'}^{i'}(\mathbf{x}')) = c_q(\mathbf{x}, \mathbf{x}'|\boldsymbol{\theta}_q)$ if $q = q'$ and $i = i'$, and $\text{cov}(u_q^i(\mathbf{x}), u_{q'}^{i'}(\mathbf{x}')) = 0$ otherwise. In above expressions, $\text{cov}(\cdot, \cdot)$ denotes the covariance between the two arguments. $\boldsymbol{\theta}_q$ is a vector of hyperparameters associated with each covariance function. For each fixed $q = 1, \dots, Q$, the $u_q^i(\mathbf{x})$, $i = 1, \dots, R_q$, are independent (across i) and share the same correlation function $c_q(\mathbf{x}, \mathbf{x}'|\boldsymbol{\theta}_q)$, while the Q groups of functions $\{u_q^i\}_{q,i}$, $i = 1, \dots, R_q$, are independent of each other (i.e., across q). Setting $\mathbf{u}_q = (u_q^1(\mathbf{x}), \dots, u_q^{R_q}(\mathbf{x}))^T$ and $\mathbf{A}_q = [a_{d,q}^i] \in \mathbb{R}^{D \times R_q}$, the matrix form of (3) is:

$$\mathbf{f}(\mathbf{x}) = \sum_{q=1}^Q \mathbf{f}_q(\mathbf{x}) = \sum_{q=1}^Q \mathbf{A}_q \mathbf{u}_q(\mathbf{x}) \quad (4)$$

The cross-covariance matrix is $\text{cov}(\mathbf{f}(\mathbf{x}), \mathbf{f}(\mathbf{x}')) = \sum_{q=1}^Q \mathbf{B}_q c_q(\mathbf{x}, \mathbf{x}'|\boldsymbol{\theta}_q)$, where $\mathbf{B}_q = \mathbf{A}_q \mathbf{A}_q^T \in \mathbb{R}^{D \times D}$ are called *coregionalization matrices*. The complete set of hyperparameters in this model is $\{\boldsymbol{\theta}_q, \mathbf{B}_q\}_q$.

The challenge for LMC is in estimating the coregionalization matrices characterized by \mathbf{A}_q , which leads to several special cases. To retain the full potential of LMC while reducing the computation cost and alleviating overfitting, Higdon *et al* [4] proposed using PCA of the data $\mathbf{Y} = [\mathbf{y}_1, \dots, \mathbf{y}_M]$ to approximate \mathbf{A}_q using the first few eigenvectors. PCA leads to subspace of \mathbb{R}^D spanned by eigenvectors \mathbf{v}_q , $q = 1, \dots, r$, of the sample covariance matrix $\mathbf{Y}\mathbf{Y}^T$ corresponding to the

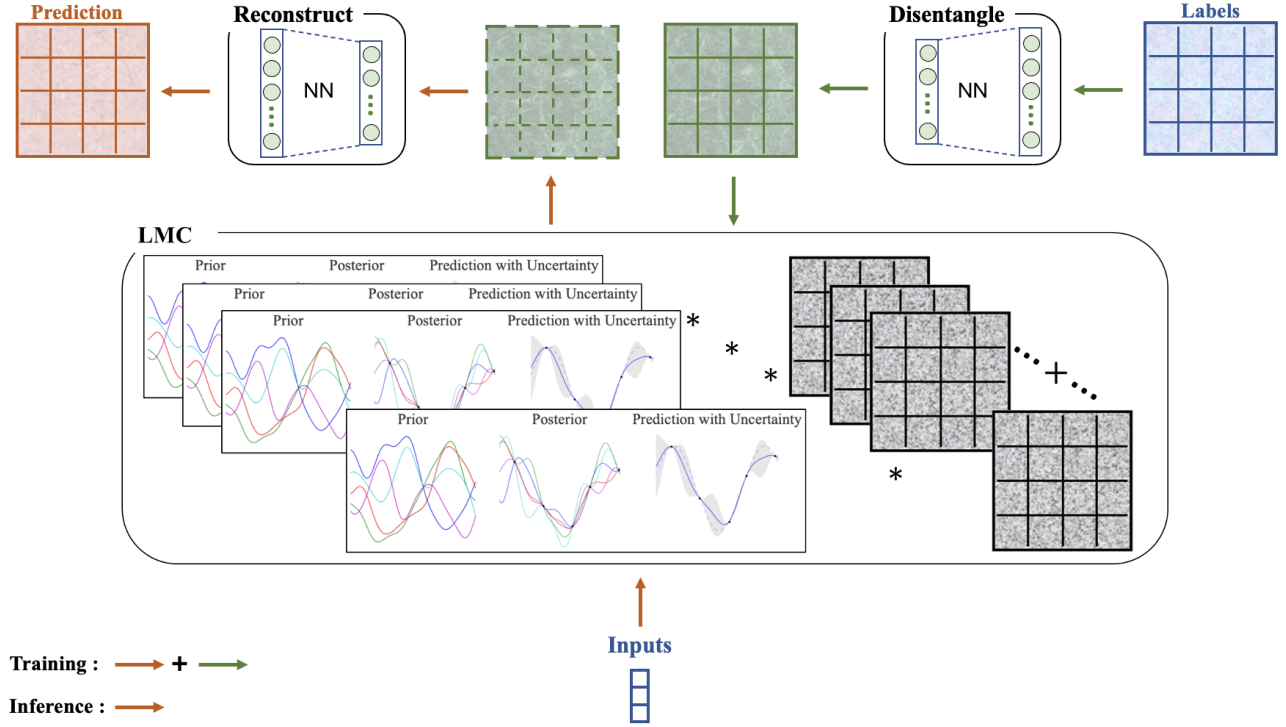


Fig. 1: The architecture of E-LMC.

first $r < D$ eigenvalues (provided the eigenvalues are arranged in a non-increasing order). This suggests a model of the form (4) with $Q = r$, $R_q = 1$ and $\mathbf{A}_q = \mathbf{v}_q$. The \mathbf{u}_q are scalar, independent GPs $u_q(\mathbf{x})$ that can be learned using the principal components obtained from the data [34].

E. Multilayer Perceptron

To harness stronger spatial output correlations and bring more scalability to LMC, we employ the neural network to capture the nonlinear features. Specifically, we use MLP, which is composed of multiple fully-connected layers. Similar to an autoencoder, this module's output attempts to be as close as possible to its input and calculates an error. The error is used to adjust the weights by back-propagation and gradient descent algorithms.

The learning process for this module is composed of two stages: *disentangle* and *reconstruct*. The disentangle process occurs between the input layer and the LMC, extracting nonlinear features while leaving linear features. This is given by (5).

$$\mathbf{h} = \text{ReLU}(\mathbf{b} + \mathbf{W}\mathbf{y}) \quad (5)$$

where \mathbf{W} and \mathbf{b} stand for the weight matrix and bias in the disentangle process; \mathbf{y} denotes the input; \mathbf{h} is the output for LMC.

The reconstruct process entails the reconstruction of nonlinear features from the LMC. The process to obtain the output is given by (6).

$$\hat{\mathbf{y}} = \text{ReLU}(\mathbf{b}' + \mathbf{W}'\mathbf{h}') \quad (6)$$

where \mathbf{W}' and \mathbf{b}' stand for the weight matrix and bias in the reconstruct process; \mathbf{h}' denotes the input from LMC; $\hat{\mathbf{y}}$ is the output.

As previously mentioned, the reconstruct step tries to rebuild the disentangled data by comparing the obtained output with the original input. In order to evaluate this, we implement mean square error (MSE) as the loss function.

F. Training and Inference of E-LMC

So far, we have introduced the skeleton of our E-LMC model. The challenge is the optimization of model parameters.

The training and inference algorithms are shown in Algorithm 1 and Algorithm 2, respectively. Training includes the whole MLP module and the LMC module. Inference includes the reconstruct process of the MLP module and the LMC module. \mathbf{X} represents the low-dimensional inputs. \mathbf{Y} represents the high-dimensional spatial outputs. \mathbf{Y}' represents the high-dimensional spatial predictions. \mathbf{Z} represents the latent features/bases of the outputs. \mathbf{W}_D and \mathbf{W}_R are learnable weights in MLP. μ and Σ are learnable means and covariances in GP.

Algorithm 1: Training on E-LMC

```
1 initialization on MLP;
2 for number of training iterations do
3   for number of batches of the training dataset do
4      $\text{MLP}(\mathbf{Y}, W_D) \rightarrow \mathbf{M}$ 
5      $\text{PCA}(\mathbf{M}) \rightarrow \mathbf{Z}$ 
6      $\text{InversePCA}(\mathbf{Z}) \rightarrow \mathbf{M}'$ 
7      $\text{MLP}(\mathbf{M}', W_R) \rightarrow \mathbf{Y}'$ 
8     Update MLP parameters  $W_D$  and  $W_R$ 
9     through gradient descent.
10  end
11 end
12 initialization on GP;
13 for number of training iterations do
14    $\text{GP}(\mathbf{X}, \mu, \Sigma) \rightarrow \mathbf{Z}$ 
15   Update GP parameters through gradient descent.
16 end
```

Algorithm 2: Inference on E-LMC

```
1 for number of testing iterations do
2   for number of batches of the testing dataset do
3      $\text{GP}(\mathbf{X}, \mu, \Sigma) \rightarrow \mathbf{Z}$ 
4      $\text{InversePCA}(\mathbf{Z}) \rightarrow \mathbf{M}'$ 
5      $\text{MLP}(\mathbf{M}', W_R) \rightarrow \mathbf{Y}'$ 
6   end
7 end
```

IV. EXPERIMENTS

A. Datasets

In order to assess the performance of E-LMC, two representative real-world physics-based datasets are used.

The first is the cantilever beam dataset. This dataset is about the structural topology optimization of a cantilever beam, shown in Fig. 2. Structural topology optimization is a mathematical method that optimizes material distribution within given simulation parameters [35]. It is typically associated with a large number of simulation parameters and needs a high computation cost. Cantilever beams are material structures that have the maximum stiffness when bearing forces from the right side. There are three simulation parameters, namely, the location of point load P_1 , the angle of point load P_2 , and the filter radius P_3 [36]. The simulation triplet $P = (P_1 \in [-20, 20], P_2 \in [0, \pi], P_3 \in [1.1, 2.5])$ is the input, while the 40×80 image presents the field output [37].

The second is the metal melting front dataset. A square cavity containing liquid and solid contents is subjected to a temperature difference between the left and right boundaries [38]. The fluid and solid phases are considered to be separate domains sharing a moving melting front. The liquid velocity is recorded on a 100×100 square spatial grid as outputs, and the corresponding inputs are three-dimensional.

We consider the cantilever beam and metal melting front as effective demonstrations for E-LMC because of their high-dimensional spatial outputs.

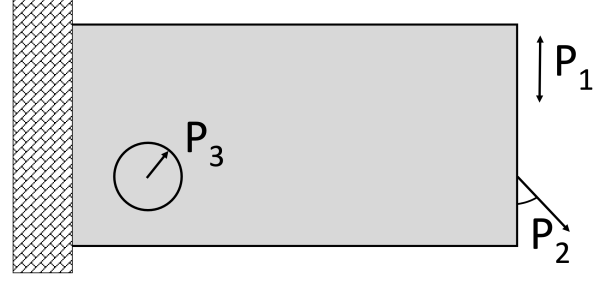


Fig. 2: The geometry and external forces for a cantilever beam.

B. Baselines

In order to comprehensively evaluate the performance of E-LMC, we compare with the MLP model and the GP-based models:

- **MLP**: This end-to-end deep learning model using fully-connected neural networks predicts the high-dimensional spatial outputs directly from the low-dimensional inputs.
- **LMC (PCA-GP)** [4]: This multi-output GP regression approach generates the outputs via a linear combination of fixed bases. PCA is used to derive the bases from the training samples.
- **Isomap-GP** [5]: This method exploits patterns in the permissible output space using manifold learning. Isomap and kernel Isomap are used to significantly reduce the dimensionality of the output space to construct a GP emulator efficiently.
- **kPCA-GP** [6]: This is a cogenetic method similar to Isomap-GP. The kernel PCA and diffusion maps are developed to reduce the dimensionality of outputs.
- **HOGP** [15]: This high-order GP regression model can flexibly capture complex correlations among the outputs and naturally scale up to high-dimensional outputs.

C. Experimental Settings

For E-LMC, we organize the outputs from the cantilever beam and metal melting front datasets into images with sizes of 40×80 and 100×100 , respectively. The model is built based on the PyTorch and GPyTorch frameworks. We adapt 10 fully-connected layers for the MLP module, and the number of units for each hidden layer is $\{4096, 8192, 4096, 3200, 3200, 4096, 8192, 4096\}$. We use the RBF squared exponential kernel for GP in the LMC module. We employ the latent features/bases *rank*, and vary *rank* from $\{1, 2, 5, 10\}$. We use Adam as the optimizer with learning rate as 0.001 and set the batch size as 64.

For MLP, We adapt 10 fully-connected layers in our model, and the number of units for each hidden layer is $\{8, 16, 32, 64, 128, 256, 512, 1024, 2048\}$. We use Adam as the optimizer with learning rate as 0.001 and set the batch size as 32.

For HOGP, PCA-GP, Isomap-GP, and kPCA-GP, we vary the number of latent features $rank$ from $\{1, 2, 5, 10\}$ as well. We use the ARD squared exponential kernel for the GP parts and the same initialization for the kernel parameters and the inverse variance. These four baselines are implemented with MATLAB 2019. We use Adam as the optimizer with learning rate as 0.001.

From the cantilever beam dataset, we randomly select $\{10, 50, 100, 500, 1000\}$ samples for training, and from the remaining data for testing. From the metal melting front dataset, we randomly select $\{10, 50, 100\}$ samples for training, and from the remaining data for testing. We report the average results over 5 random shuffling testing datasets. We use the mean square error (MSE) as metrics in our experiments.

D. Results

As shown in Fig. 3, E-LMC achieves significant improvements over all the baseline methods by a substantial margin in MSE. Generally, the prediction accuracies of almost all the methods are close when the size of training set is small. When the training size increases over 100, E-LMC, HOGP, and MLP show evident improvements over all the competing methods. The explanation for this phenomenon might be that the training set is too small to provide useful information at the start, leading to poor prediction performance. When the size of training samples increases, E-LMC can capture complicated output correlations and exhibit superior prediction accuracy. While LMC doesn't show as strong data-driven property as E-LMC. In summary, E-LMC has the stability in GP surrogate models for small datasets and the data-driven property in neural networks for large datasets.

The comparison results for 10 latent features are presented in Table I. Specifically, E-LMC outperforms the state-of-the-art algorithm by 14.4% on 1000 training samples from cantilever beam dataset and 40% on 100 training samples from metal melting front dataset.

To allow for a fine-grained comparison, we visualize 7 predictions from cantilever beam dataset and 3 predictions from metal melting front dataset by all the methods (the number of latent features is set to 10, and the number of training samples is set to 1000), as well as the ground-truth. All of the chosen samples are representative of the corresponding datasets. As illustrated in Fig. 4, on the cantilever beam dataset, the structures predicted by E-LMC are closest to the ground-truth. Specifically, predictions by LMC (PCA-GP) usually have blurred structures. HOGP, kPCA-GP, and Isomap-GP yield clearer local structures. MLP cannot deal with a variety of forms, and the local details sometimes diverge greatly from the ground-truth (see the second, third, and seventh structures in Fig. 4e). This vividly demonstrates that the neural network is prone to overfitting between high-dimensional outputs and low-dimensional inputs from a relatively small dataset. In contrast, E-LMC alleviates the overfitting issue by combining neural network with LMC.

In Fig. 5, it is worth noticing that HOGP and MLP are not very stable when the number of latent functions is set to 1 (see

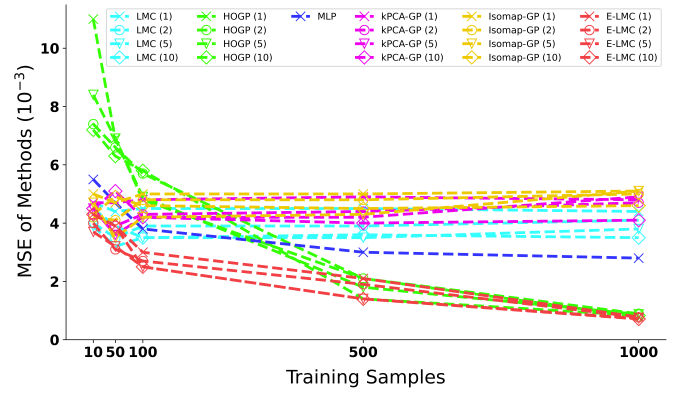


Fig. 3: The MSE on cantilever beam dataset w.r.t different sizes of training set. Numbers in the legend indicate the number of latent features for E-LMC, LMC (PCA-GP), HOGP, kPCA-GP, and Isomap-GP.

Fig. 5a, 5b, 5c, 5f). For example, in Fig. 5f, the average MSE of MLP turns out to be far greater than all the other methods. In contrast, our E-LMC performs effectively even when only taking 1 latent feature.

TABLE I
Comparison Results with Baselines on Datasets ($rank = 10$)

Dataset	Training Samples	MSE of Methods					
		<i>E-LMC</i>	<i>LMC (PCA-GP)</i>	<i>HOGP</i>	<i>MLP</i>	<i>kPCA-GP</i>	<i>Isomap-GP</i>
Cantilever Beam	10	4.3×10^{-3}	4.5×10^{-3}	7.2×10^{-3}	5.5×10^{-3}	4.5×10^{-3}	4.3×10^{-3}
	50	3.9×10^{-3}	3.9×10^{-3}	6.3×10^{-3}	4.7×10^{-3}	5.1×10^{-3}	4.9×10^{-3}
	100	2.5×10^{-3}	3.5×10^{-3}	5.8×10^{-3}	3.8×10^{-3}	4.2×10^{-3}	4.6×10^{-3}
	500	1.4×10^{-3}	3.6×10^{-3}	1.4×10^{-3}	3.0×10^{-3}	4.0×10^{-3}	4.5×10^{-3}
	1000	7.1×10^{-4}	3.5×10^{-3}	8.3×10^{-4}	2.8×10^{-3}	4.1×10^{-3}	4.6×10^{-3}
Metal Melting Front	10	1.4×10^{-5}	2.2×10^{-5}	6.4×10^{-5}	8.2×10^{-5}	2.0×10^{-5}	1.8×10^{-5}
	50	4.1×10^{-6}	4.2×10^{-6}	5.8×10^{-6}	8.0×10^{-6}	4.9×10^{-6}	4.5×10^{-6}
	100	2.1×10^{-6}	3.9×10^{-6}	4.9×10^{-6}	3.8×10^{-6}	3.5×10^{-6}	3.5×10^{-6}

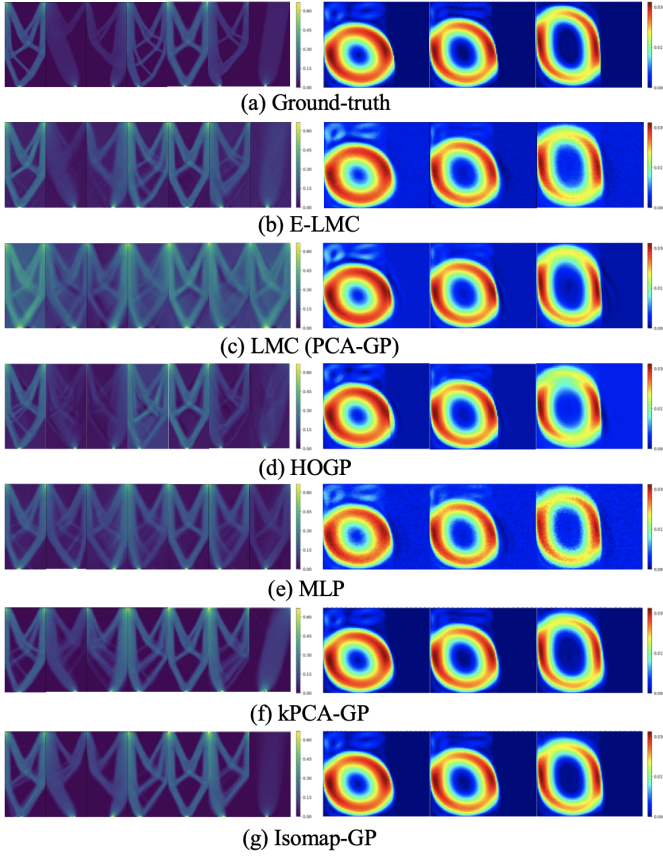


Fig. 4: The predicted topology structures for cantilever beam dataset (left) and the predicted metal conditions for metal melting front dataset (right). The number of latent features for E-LMC, LMC (PCA-GP), HOGP, kPCA-GP, and Isomap-GP were set to 10. Models were trained on 1000 training samples for cantilever beam dataset and 100 training samples for metal melting front dataset.

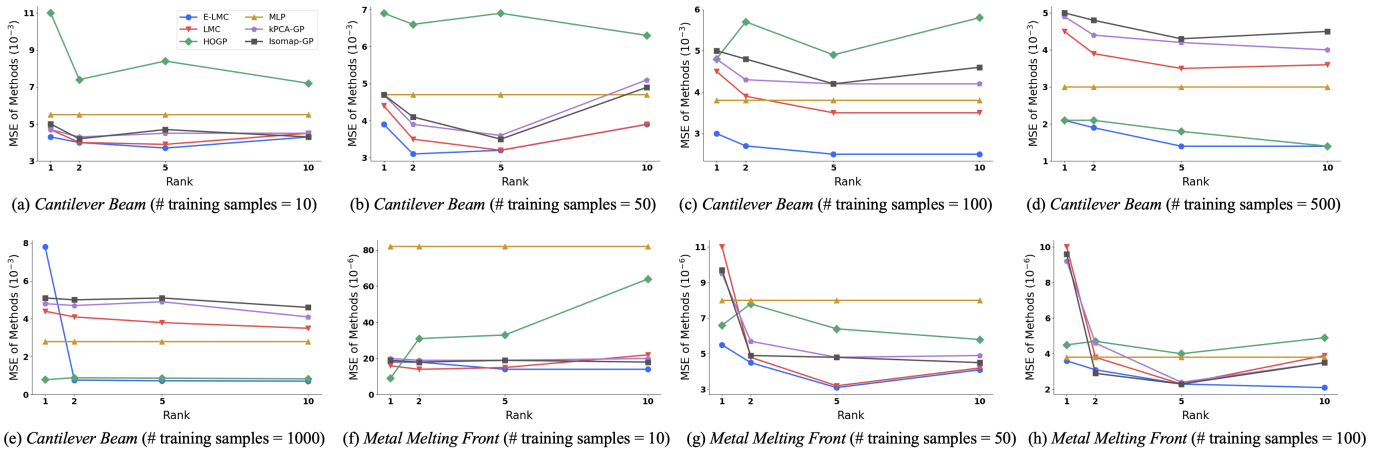


Fig. 5: The y-axis represents the MSE of all the methods on 2 small datasets. The x-axis represents the number of latent features for E-LMC, LMC (PCA-GP), HOGP, kPCA-GP, and Isomap-GP.

V. CONCLUSION

In this paper, we propose an extended linear model of coregionalization (E-LMC) for the predictions of spatial fields. We introduce an invertible neural network to linearize the highly complex and nonlinear correlations among spatial fields and cooperate with LMC to map low-dimensional inputs to high-dimensional outputs, based on a small dataset. Real-world experiments demonstrate that E-LMC can exploit spatial correlations effectively, showing a maximum improvement of about 40% over the other state-of-the-art spatial field models.

ACKNOWLEDGMENT

The authors would like to acknowledge the computation supports from Shucheng Ye and Yinpeng Wu of Beihang University.

REFERENCES

- [1] I. Bilonis, N. Zabarar, B. A. Konomi, and G. Lin, "Multi-output separable gaussian process: Towards an efficient, fully bayesian paradigm for uncertainty quantification," *Journal of Computational Physics*, vol. 241, pp. 212–239, 2013.
- [2] A. Keane and P. Nair, *Computational approaches for aerospace design: the pursuit of excellence*. John Wiley & Sons, 2005.
- [3] M. C. Kennedy and A. O'Hagan, "Predicting the output from a complex computer code when fast approximations are available," *Biometrika*, vol. 87, no. 1, pp. 1–13, 2000.
- [4] D. Higdon, J. Gattiker, B. Williams, and M. Rightley, "Computer model calibration using high-dimensional output," *Journal of the American Statistical Association*, vol. 103, no. 482, pp. 570–583, 2008.
- [5] W. Xing, A. A. Shah, and P. B. Nair, "Reduced dimensional gaussian process emulators of parametrized partial differential equations based on isomap," *Proceedings of the Royal Society A: Mathematical, Physical and Engineering Sciences*, vol. 471, no. 2174, p. 20140697, 2015.
- [6] W. W. Xing, V. Triantafyllidis, A. A. Shah, P. Nair, and N. Zabarar, "Manifold learning for the emulation of spatial fields from computational models," *Journal of Computational Physics*, vol. 326, pp. 666–690, 2016.
- [7] I. Macedo and R. Castro, "Learning div-free and curl-free vector fields by matrix-valued kernels," 2010.
- [8] A. Shah, W. Xing, and V. Triantafyllidis, "Reduced-order modelling of parameter-dependent, linear and nonlinear dynamic partial differential equation models," *Proceedings of the Royal Society A: Mathematical, Physical and Engineering Sciences*, vol. 473, no. 2200, p. 20160809, 2017.
- [9] R. K. Tripathy and I. Bilonis, "Deep uq: Learning deep neural network surrogate models for high dimensional uncertainty quantification," *Journal of computational physics*, vol. 375, pp. 565–588, 2018.
- [10] C. Nentwich and S. Engell, "Application of surrogate models for the optimization and design of chemical processes," in *2016 International Joint Conference on Neural Networks (IJCNN)*. IEEE, 2016, pp. 1291–1296.
- [11] N. Takeishi, Y. Kawahara, and T. Yairi, "Learning koopman invariant subspaces for dynamic mode decomposition," *arXiv preprint arXiv:1710.04340*, 2017.
- [12] A. G. Wilson, Z. Hu, R. Salakhutdinov, and E. P. Xing, "Deep kernel learning," in *Artificial intelligence and statistics*. PMLR, 2016, pp. 370–378.
- [13] A. G. Wilson, D. A. Knowles, and Z. Ghahramani, "Gaussian process regression networks," *arXiv preprint arXiv:1110.4411*, 2011.
- [14] D. Crevellén-García, "Surrogate modelling for the prediction of spatial fields based on simultaneous dimensionality reduction of high-dimensional input/output spaces," *Royal Society open science*, vol. 5, no. 4, p. 171933, 2018.
- [15] S. Zhe, W. Xing, and R. M. Kirby, "Scalable high-order gaussian process regression," in *The 22nd International Conference on Artificial Intelligence and Statistics*. PMLR, 2019, pp. 2611–2620.
- [16] W. W. Xing, R. M. Kirby, and S. Zhe, "Deep coregionalization for the emulation of simulation-based spatial-temporal fields," *Journal of Computational Physics*, vol. 428, p. 109984, 2021.
- [17] C. Lu and X. Tang, "Surpassing human-level face verification performance on lfw with gaussianface," in *Twenty-ninth AAAI conference on artificial intelligence*, 2015.
- [18] H. Kim, X. Lu, S. Flaxman, and Y. W. Teh, "Collaborative filtering with side information: a gaussian process perspective," *arXiv preprint arXiv:1605.07025*, 2016.
- [19] J. Snoek, H. Larochelle, and R. P. Adams, "Practical bayesian optimization of machine learning algorithms," *Advances in neural information processing systems*, vol. 25, 2012.
- [20] D. Higdon, "Space and space-time modeling using process convolutions," in *Quantitative methods for current environmental issues*. Springer, 2002, pp. 37–56.
- [21] P. Boyle and M. Frean, "Dependent gaussian processes," *Advances in neural information processing systems*, vol. 17, pp. 217–224, 2005.
- [22] J. McFarland, S. Mahadevan, V. Romero, and L. Swiler, "Calibration and uncertainty analysis for computer simulations with multivariate output," *AIAA journal*, vol. 46, no. 5, pp. 1253–1265, 2008.
- [23] P. Ray, S. S. Reddy, and T. Banerjee, "Various dimension reduction techniques for high dimensional data analysis: a review," *Artificial Intelligence Review*, pp. 1–43, 2021.
- [24] I. T. Jolliffe and J. Cadima, "Principal component analysis: a review and recent developments," *Philosophical Transactions of the Royal Society A: Mathematical, Physical and Engineering Sciences*, vol. 374, no. 2065, p. 20150202, 2016.

- [25] X. Kong, X. Liu, R. Shi, and K. Y. Lee, "Wind speed prediction using reduced support vector machines with feature selection," *Neurocomputing*, vol. 169, pp. 449–456, 2015.
- [26] B. G. Cambuí, R. G. Mantovani, and R. Cerri, "Exploring autoencoders for feature extraction in multi-target classification," in *2021 International Joint Conference on Neural Networks (IJCNN)*. IEEE, 2021, pp. 1–8.
- [27] G. T. Reddy, M. P. K. Reddy, K. Lakshmana, R. Kaluri, D. S. Rajput, G. Srivastava, and T. Baker, "Analysis of dimensionality reduction techniques on big data," *IEEE Access*, vol. 8, pp. 54 776–54 788, 2020.
- [28] F. Zhu, S. Xie, J. Xu, and H. He, "Various artifacts reduction algorithms for eeg recorded in continuous fmri scan environment," in *The 2012 International Joint Conference on Neural Networks (IJCNN)*. IEEE, 2012, pp. 1–4.
- [29] G. E. Hinton and R. R. Salakhutdinov, "Reducing the dimensionality of data with neural networks," *science*, vol. 313, no. 5786, pp. 504–507, 2006.
- [30] H. Bourlard and Y. Kamp, "Auto-association by multilayer perceptrons and singular value decomposition," *Biological cybernetics*, vol. 59, no. 4, pp. 291–294, 1988.
- [31] M. Seuret, M. Alberti, M. Liwicki, and R. Ingold, "Pca-initialized deep neural networks applied to document image analysis," in *2017 14th IAPR international conference on document analysis and recognition (ICDAR)*, vol. 1. IEEE, 2017, pp. 877–882.
- [32] P. Krähenbühl, C. Doersch, J. Donahue, and T. Darrell, "Data-dependent initializations of convolutional neural networks," *arXiv preprint arXiv:1511.06856*, 2015.
- [33] C. Rasmussen and C. Williams, "Gaussian processes for machine learning.,(mit press: Cambridge, ma)," 2006.
- [34] W. Xing, F. Yu, P. Leung, X. Li, P. Wang, and A. Shah, "A new multi-task learning framework for fuel cell model outputs in high-dimensional spaces," *Journal of Power Sources*, vol. 482, p. 228930, 2021.
- [35] M. P. Bendsoe and O. Sigmund, *Topology optimization: theory, methods, and applications*. Springer Science & Business Media, 2003.
- [36] T. E. Bruns and D. A. Tortorelli, "Topology optimization of non-linear elastic structures and compliant mechanisms," *Computer methods in applied mechanics and engineering*, vol. 190, no. 26-27, pp. 3443–3459, 2001.
- [37] W. Xing, S. Y. Elhabian, V. Keshavarzadeh, and R. M. Kirby, "Shared-gaussian process: Learning interpretable shared hidden structure across data spaces for design space analysis and exploration," *Journal of Mechanical Design*, vol. 142, no. 8, p. 081707, 2020.
- [38] F. Wolff and R. Viskanta, "Solidification of a pure metal at a vertical wall in the presence of liquid superheat," *International journal of heat and mass transfer*, vol. 31, no. 8, pp. 1735–1744, 1988.